



N-doped two-dimensional ultrathin NiO nanosheets for electrochromic supercapacitor

Junying Xue¹, Shen Wang¹, Hongming Zhang¹, Ying Song^{1,*}, Yao Li^{2,*} , and Jiupeng Zhao^{1,*} 

¹School of Chemistry and Chemical Engineering, Harbin Institute of Technology, Harbin 150001, People's Republic of China

²Center for Composite Materials and Structure, Harbin Institute of Technology, Harbin 150001, People's Republic of China

Received: 26 July 2020

Accepted: 30 September 2020

© Springer Science+Business Media, LLC, part of Springer Nature 2020

ABSTRACT

The performance of electrochromic supercapacitors (ESCs) can be improved by the use of electrodes with high electronic conductivity and ion transport ability. Herein, two-dimensional (2D) N-doped NiO ultrathin nanosheets (N-NiO UTNSs) synthesized in situ on fluorine-doped tin oxide glass were used as bifunctional ESC electrodes. These electrodes exhibited an elevated specific capacitance (540 F g^{-1} at 1 A g^{-1}), superior cycling stability (85% capacitance retention after 10,000 cycles), and good electrochromic properties (color change from colorless to black with a transmittance modulation of 73% and a coloration efficiency of up to $83.47 \text{ cm}^2 \text{ C}^{-1}$ at 550 nm), which was ascribed to the high electronic conductivity of NiO (due to N doping) and the short ion diffusion path (due to the ultralow nanosheet thickness). To further explore the practical applications of N-NiO UTNSs, we constructed asymmetric ESCs by integrating NiO films with Fe_2O_3 films and revealed that these devices displayed applied voltage-dependent colors. Two charged asymmetric ESCs connected in series could light up a red light-emitting diode and changed color synchronously with charge state alteration. Thus, our results contribute to the development of Ni-based electrochromic supercapacitors exhibiting charge state-dependent color changes.

1 Introduction

Electrochromism is a phenomenon which the color of a material changed reversibility simultaneous insertion/extraction of ions. With the advent of electronic device intellectualization, much effort has been directed at the realization of novel personalized

electrochromic supercapacitors in line with the general trend observed in the field of science and technology [1]. The working mechanism and structure of supercapacitors are similar to those of electrochromic indicators, which allows the fabrication of bifunctional electrochromic supercapacitors (ESCs) exhibiting visually discernible (dis)charge state-dependent color changes [2–4]. In this context, inorganic

Address correspondence to E-mail: songy@hit.edu.cn; yaoli@hit.edu.cn; jpzhao@hit.edu.cn

transition metal oxides (TMOs) featuring both capacitive and electrochromic properties, e.g., WO_3 [5], V_2O_5 [6], TiO_2 [7], and NiO [8], have been vigorously researched as ESC components.

Despite the realization of several prototypical ESCs with TMO electrodes, their further development is hindered by (i) the sluggish ion transport kinetics due to the slow insertion/extraction and diffusion of ions in bulk materials (which leads to low rate capability, transmittance modulation, and coloration/bleaching response) [9, 10] and (ii) the high resistance of most TMO electrodes [11]. These obstacles can be overcome using several strategies such as material nanostructure design, doping, and hybridization with complementary materials [12–14]. In particular, two-dimensional (2D) nanosheets are considered to be ideal frameworks for fast ion transport because of their large active surface area, open spaces, and shortened diffusion path [15]. However, individual 2D nanosheets easily undergo tight irreversible restacking to reduce their surface free energy and form aggregates, which decreases active surface area and hinders dynamical ion diffusion [16]. In addition, suitable nanoarchitectures with electrically conductive additives (e.g., graphene, carbon nanotubes, and conducting polymers) can be employed to improve TMO conductivity [17]. However, this method does not allow one to change the intrinsic properties of TMOs, and the use of some dark-colored additives may remarkably deteriorate electrochromic performance, e.g., by affecting transmittance modulation. N doping has been reported as an alternative strategy for improving the intrinsic electronic conductivity of TMOs [18]. For example, Yu et al. reported that N doping of Co_3O_4 results in enhanced electronic conductivity, and, hence, elevated catalytic activity [19], while Choi et al. showed that N-doped NiCo_2O_4 nanowires exhibit elevated electrical conductivity [20]. However, these N doping methods are time- and energy-consuming, involve multiple steps, and require the use of an NH_3 atmosphere or NH_3 plasma treatment. Therefore, simple and effective routes to 2D nanosheet-based N-doped bifunctional electrode materials are highly sought after.

Herein, arrays of 2D N-doped NiO ultrathin nanosheets (N- NiO UTNSs) directly anchored on fluorine-doped tin oxide (FTO) substrates were fabricated by a single-step solvothermal process followed by simple annealing and exhibited high supercapacitor and electrochromic performances.

The corresponding electrode featured an specific capacitance of 540 F g^{-1} at 1 A g^{-1} and retained 85% of its initial capacitance after 10,000 cycles, while film transmittance modulation reached 73%, and coloration efficiency at 550 nm was as high as $83.47 \text{ cm}^2 \text{ C}^{-1}$. Additionally, the prepared nanosheets were used to construct an asymmetric ESC (AESC) that changed color when the applied voltage was increased from 0 to 1.7 V. Two AESCs connected in series could light up a light-emitting diode and synchronously changed color upon discharge, which highlighted the successful realization of bifunctional ESCs.

2 Experimental

2.1 Synthesis of 2D N- NiO UTNS arrays

Networked 2D N- NiO UTNS arrays were synthesized as follows. FTO glass was cleaned by sequential ultrasonication in deionized water, acetone, and ethanol, dried at $60 \text{ }^\circ\text{C}$ for 2 h, treated with plasma for 5 min in air to increase surface hydrophilicity, and put into a Teflon autoclave. Solutions of nickel nitrate (0.5 g) and 2-methyl-imidazole (0.6 g) in methanol were mixed, stirred, and transferred to the Teflon autoclave, which was then sealed and heated at $120 \text{ }^\circ\text{C}$ for 4 h. Subsequently, the FTO glass was taken out from the autoclave and washed with methanol for three times to remove the solvent and products loosely attached on the surface. Finally, the FTO glass with loaded products was dried and annealed at $300 \text{ }^\circ\text{C}$ in air for 2 h to afford crystalline 2D NiO UTNSs. For comparison, FTO glass with loaded products was also annealed at $400 \text{ }^\circ\text{C}$ for 2 h to afford nanosheets denoted as NiO-NS 400 .

2.2 AESC fabrication

AESCs ($2 \times 2 \text{ cm}$) were fabricated using 2D N- NiO UTNS-coated FTO glass as the positive electrode and Fe_2O_3 film-coated FTO glass as the negative electrode. The preparation and characterization of Fe_2O_3 are described in the Supporting Information (Fig. S1). A nylon membrane soaked in 1 M KOH was used as the separator and electrolyte. The assembled device was sealed with a UV-curing adhesive.

2.3 Characterization

The phase compositions of the samples were detected by X-ray diffractometer (XRD, Japan Rigaku). The morphology and structure were characterized by scanning electron microscopy (SEM, Zeiss), transmission electron microscopy (TEM, JEOL 2010), high-resolution transmission electron microscopy (HRTEM, JEOL 2010), and selected area electron diffraction (SAED, JEOL 2010) and atomic force microscopy (AFM, Bruker). UV–Vis spectra (PGeneral TU-1810 UV–vis spectrophotometer) were used to study the bandgap properties with a Varian Cary 5G spectrometer between 300 to 1200 nm. X-ray photoelectron spectroscopy (XPS Thermo Fisher, E. Grinstead, UK) was recorded using Al K α irradiation as the excitation source.

2.4 Electrochemical and electrochromic measurements

The electrochemical properties of the samples were investigated by an electrochemical workstation (CHI 660E, chenhua) with a three-electrode configuration, where the 2D N-NiO UTNSs on FTO glass, Pt foil, and Hg/HgO electrode served as the working electrode, the counter electrode, and the reference electrode, respectively. 1 M KOH was used as the electrolyte. In situ electrochromic performance of the samples in response to the charge and discharge processes was measured by using an Ocean Optics (MAYA 2000-Pro) spectrometer in combination with an electrochemical workstation.

3 Result and discussion

The solvothermal fabrication of 2D N-NiO UTNSs is schematically presented in Scheme 1. Figure 1a and b show the X-ray diffraction (XRD) patterns of N-NiO UTNSs and NiO-NS 400, revealing the presence of cubic NiO (JCPDS 00-047-1049) in both cases. However, the peaks of N-NiO UTNSs were much weaker and broader than those of NiO-NS 400, i.e., the former sample comprised smaller or less crystalline grains [21]. Moreover, detailed examination of the three main diffractions peaks of NiO (Fig. 1b) indicates that the signals of N-NiO UTNSs were shifted to smaller angles relative to those of NiO-NS 400, which suggests that the former compound featured a larger

lattice constant [11, 22]. At this point, one should mention that the presence of NiO lattice defects benefits the electrochemical activity of the corresponding electrodes [23].

The elemental compositions of N-NiO UTNSs and NiO-NS 400 were probed by X-ray photoelectron spectroscopy (XPS). The survey spectra of the two samples (Fig. 1c) show that NiO-NS 400 contained Ni, O, and C, while N-NiO UTNSs additionally contained N, as follows from the observation of a peak at 399.1 eV (inset of Fig. 1c). This peak was assigned to N–Ni bonding [18] and thus confirmed N doping. Figure 1d presents high-resolution Ni 2p core-level spectra. For both samples, the peak at 853.7 eV (peak A, FWHM is 0.92) was assigned to Ni²⁺ in Ni–O bonds, whereas the peak at 855.4 eV (peak B, FWHM is 3.20) was assigned to Ni³⁺ (mainly in Ni₂O₃·H₂O, β -NiO(OH), 4Ni(OH)₂·NiOOH·xH₂O, etc.) and 860.9 eV corresponds to the satellite structure [24]. The B:A peak intensity ratios of N-NiO UTNSs and NiO-NS 400 (3.47 and 3.64, respectively) indicated that the charge transfer resistance of the former sample was lower than that of the latter [21]. It is reported that pure NiO is p-type semiconductor due to the existence of Ni³⁺ and reduce of Ni³⁺ contents could increase in hole concentration thus increase the conductivity of NiO [21, 25]. High electrical conductivity is beneficial to the reversibility and cycle stability of nickel oxide reaction. The bandgap energies of 2D N-NiO UTNS and NiO-NS 400 were calculated from the results of UV absorption measurements (Fig. S2) as 2.6 and 2.8 eV, respectively, which further confirmed that N-NiO UTNSs featured an elevated conductivity due to N doping.

The morphology of N-NiO UTNSs was probed by scanning electron microscopy (SEM). As shown in Fig. 2a, NiO had nanosheet morphology, and interconnected NiO nanosheets were evenly distributed on FTO glass. Cross-sectional SEM imaging (Fig. 2b) showed that the N-NiO UTNS film had a thickness of \sim 1 μ m, with nanosheets vertically growing on the substrate. The EDS was utilized to measure elemental composition of N-NiO UTNS film, it shows N, Ni, O, and C exists in the film (Fig. S3); this indicates that N doping exists in the films. Atomic force microscopy (AFM) imaging showed that the size of N-NiO UTNSs lied in the range of hundreds to thousands of nanometers (Fig. 2c), and the nanosheet thickness was estimated as 5 nm from the corresponding height profile (Fig. 2d). Thus, N-NiO

Scheme 1 Schematic illustration for the preparation of AESC devices

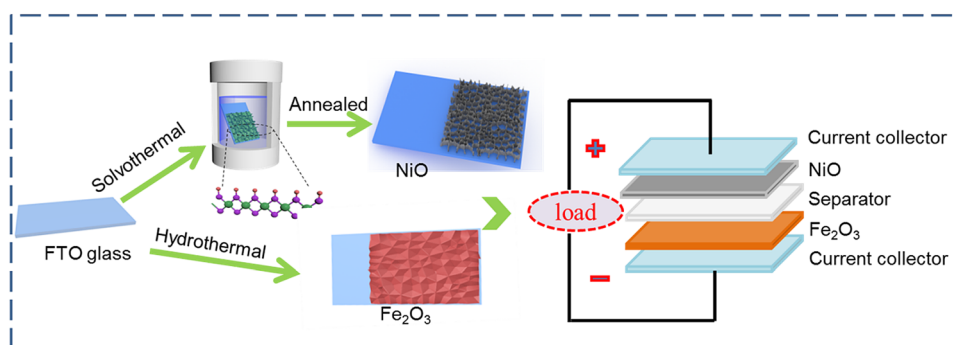
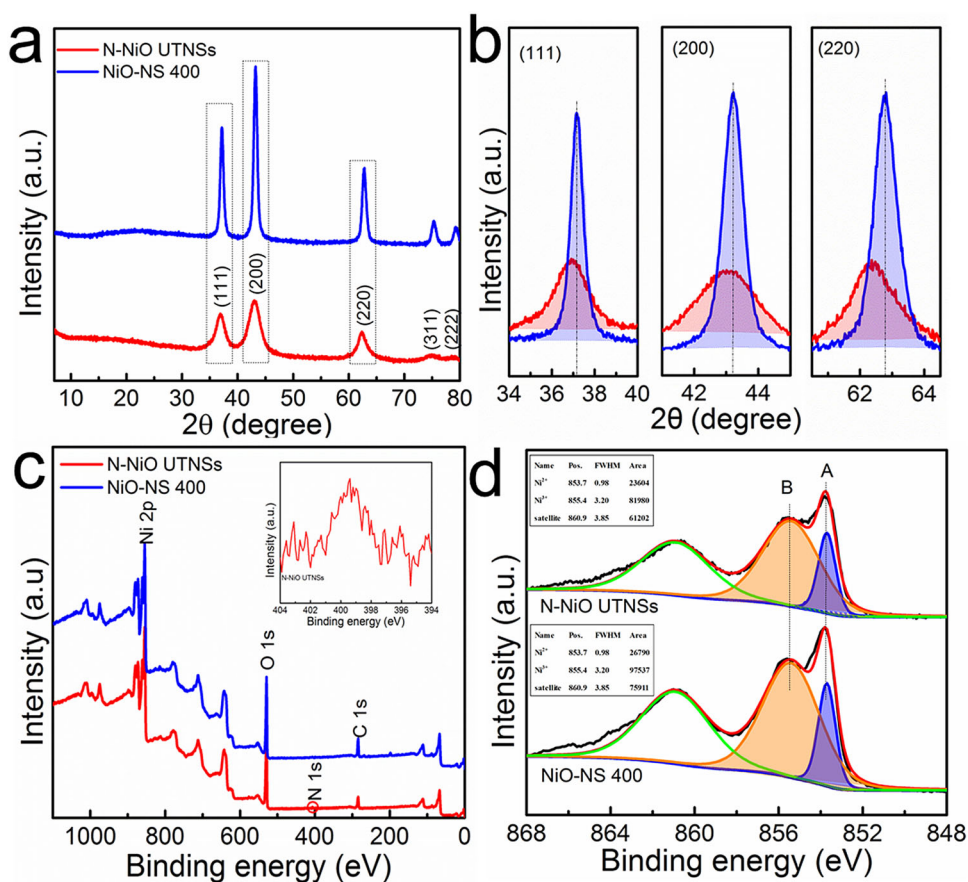


Fig. 1 **a** XRD patterns of the 2D N-NiO UTNSs and 2D NiO-NS 400; **b** Detailed view of the (111), (200) and (220) diffraction peaks in **(a)**; **c** XPS spectra of the 2D N-NiO UTNSs and 2D NiO-NS 400 (insert N 1 s); and **d** XPS spectra of Ni 2p

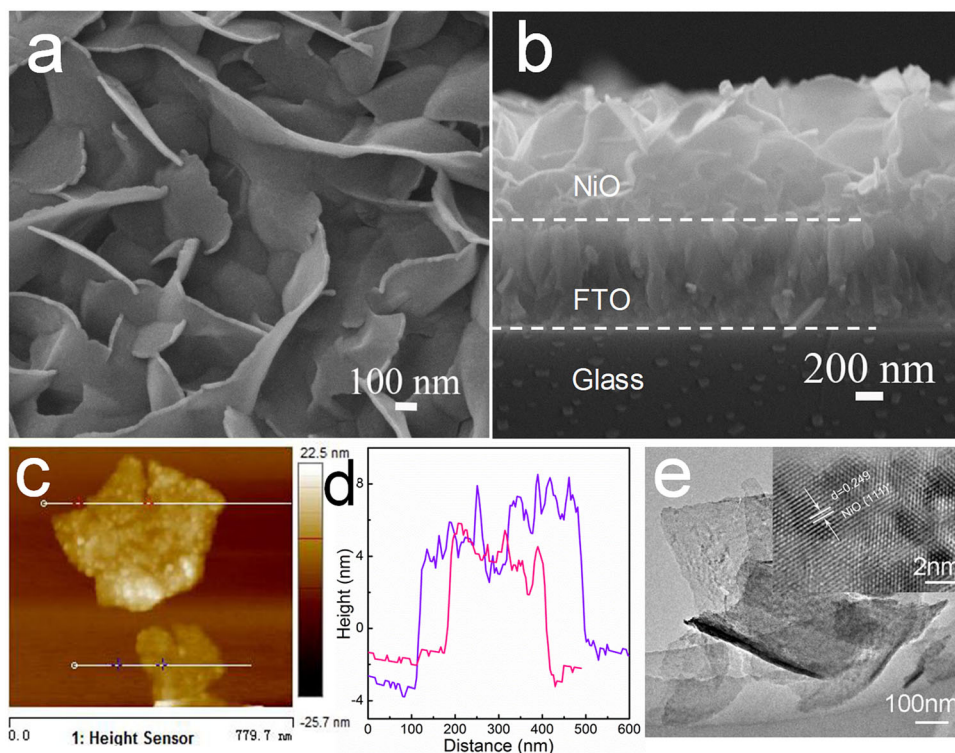


UTNSs had a large specific surface and were therefore expected to provide abundant electroactive sites and effectively facilitate electrolyte penetration and interfacial reactions [26]. The morphology of NiO-NS 400 was similar to that of N-NiO UTNSs, as shown in Figs. S4a–d. Transmission electron microscopy (TEM) imaging of N-NiO UTNSs (Fig. 2e) demonstrated that they had a particle size of hundreds to thousands of nanometers. The crystal lattice spacing ($d = 0.249$ nm) of N-NiO UTNSs indexed to the (111) plane of NiO (inset in Fig. 2e) exceeded that of NiO-

NS 400 ($d = 0.245$ nm; Fig. S4e) and was therefore expected to result in better ion diffusion and electron transfer during the redox process, thus improving electrochemical activity.

The electrochemical performances of 2D N-NiO UTNSs and 2D NiO-NS 400 were characterized by cyclic voltammetry (CV) measurements at a scan rate of 5 mV s^{-1} within a potential window of 0–0.7 V vs. Hg/HgO (Fig. 3a). Both samples showed typical redox peaks due to the pseudocapacitive behavior of NiO, and the CV curve area of N-NiO UTNSs

Fig. 2 **a** SEM image of the N-NiO UTNSs; **b** Cross-section SEM image of the N-NiO UTNSs; **c** AFM image of the N-NiO UTNSs; and **d** is the corresponding height profile along the crossed line; **e** TEM image of the N-NiO UTNSs (HRTEM is presented in the inset)



exceeded that of NiO-NS 400, which indicated that the former sample had a higher capacitance and better supercapacitor performance. Electrochemical impedance spectroscopy (EIS) measurements were performed to analyze conductivity in the frequency range of 0.01–100 kHz (Fig. 3b). The diameter of the semi-circle observed at high frequencies represented charge transfer resistance (R_{ct}), which was smaller for N-NiO UTNSs than for NiO-NS 400. The equivalent series resistance of N-NiO UTNSs was also lower than that of NiO-NS 400, i.e., the former sample had a lower impedance and better conductivity.

Electrochromic performance was characterized by recording in situ transmittance spectra under the application of a square-wave voltage in the range of -0.3 to 0.7 V vs. Hg/HgO (Fig. 3c). At 550 nm, the transmittance modulation ($\Delta T = T_b - T_c$, where T_b and T_c are the transmittances of bleached and colored states, respectively) of N-NiO UTNSs (73%) exceeded that of NiO-NS 400 (62.1%) and the bleached state of 2D N-NiO-UTNSs close to FTO glass (FTO glass transmittance is presented in Fig. S5), which was ascribed to the unique structure of N-NiO UTNSs. For high electrochromic performance, sufficient ion

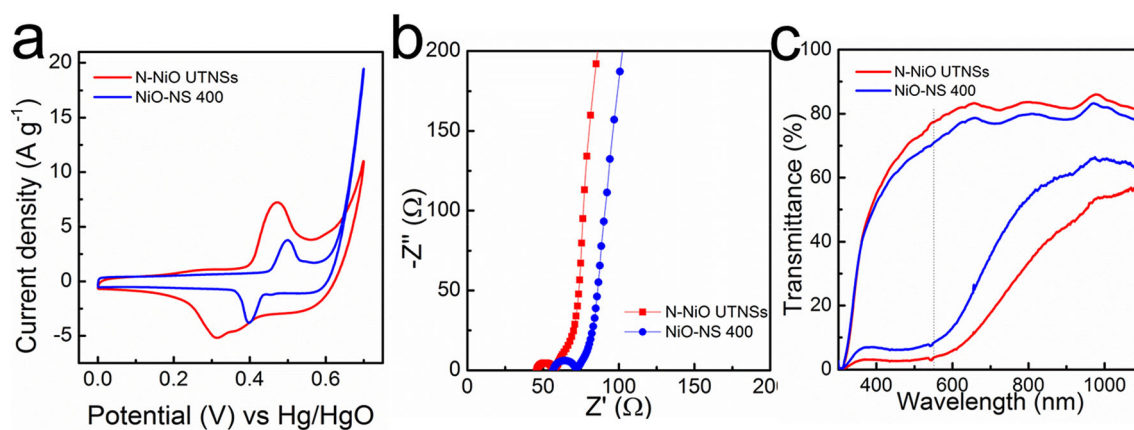


Fig. 3 **a** CV curves at 5 mV s^{-1} , **b** Nyquist plots, and **c** Transmittance spectra of the 2D N-NiO UTNSs and 2D NiO-NS 400

doping/de-doping is required to achieve efficient coloring/bleaching. Therefore, based on the above, N-NiO UTNSs were concluded to exhibit better electrochemical performance, optical properties, and conductivity than NiO-NS 400.

The electrochemical performance of N-NiO UTNSs was further probed by CV measurements at scan rates of 5–100 mV s^{-1} within a potential window of 0–0.7 V vs. Hg/HgO (Fig. 4a). All CV curves showed symmetrical redox current peaks, indicating typical pseudocapacitor faradaic interconversion of Ni^{2+} and Ni^{3+} and the excellent reversibility of this interconversion in the case of N-NiO UTNSs. Moreover, with increasing scan rate, the redox peak slightly shifted to both ends of the potential window because of the internal resistance of NiO nanosheets [8].

Galvanostatic charge/discharge testing is an important method of evaluating the electrochemical performance of electrodes. Figure 4b shows the charge/discharge curves of N-NiO UTNSs recorded at different current densities within a voltage range of 0–0.65 V, revealing that all curves showed typical asymmetry. For faradaic reactions, discharge curves include a resistive component (arising from the

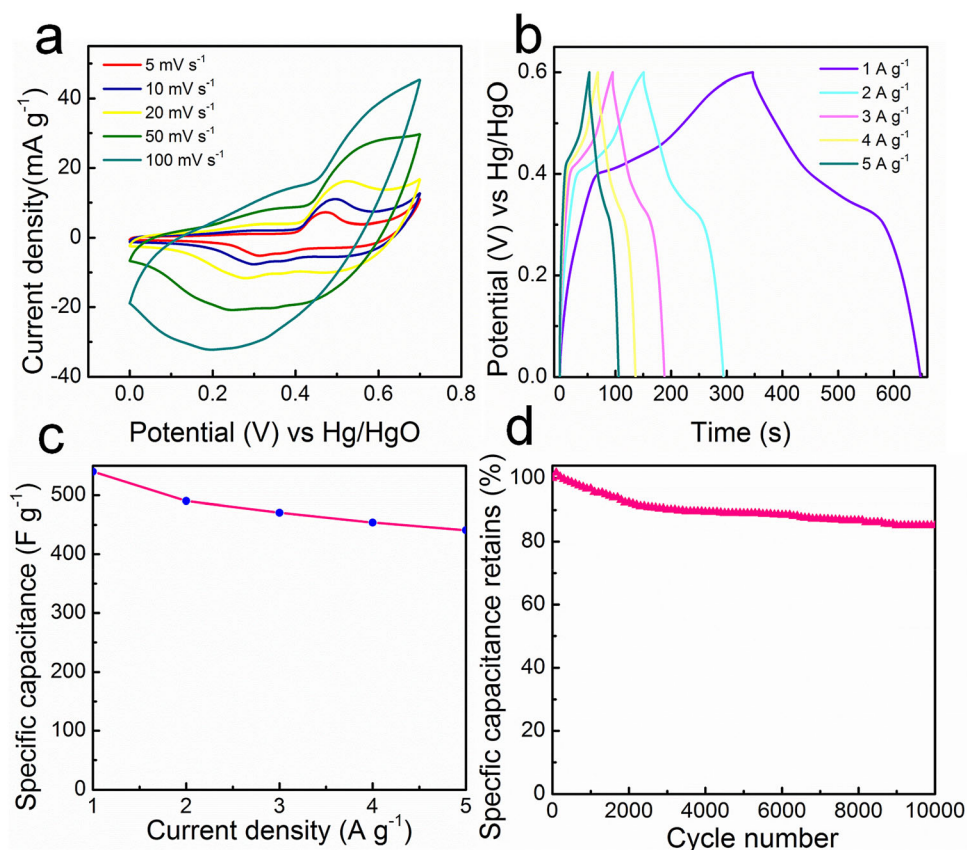
equivalent series resistance) and a capacitive component (related to the energy change-induced voltage change). The specific capacitance C of N-NiO UTNSs was calculated as [2]

$$C = \frac{I\Delta t}{m\Delta v}, \quad (1)$$

where I is the discharge current, m is the weight of the active material, Δv is the potential window, and Δt is the total discharge time. C values of 540, 490.3, 470.5, 454, and 440.8 F g^{-1} were obtained for NiO UTNSs at current densities of 1, 2, 3, 4, and 5 A g^{-1} , respectively (Fig. 4c).

The cycling stability of the N-NiO UTNS electrode was investigated at a current density of 3 A g^{-1} over 10,000 charge–discharge cycles (Fig. 4d), and a capacitance retention of 85% was obtained. The drop of capacitance upon charge/discharge cycling may result from bulging due to the continual intercalation/deintercalation of ions into/from the electrode. Imaging of cycled N-NiO UTNSs showed that the 2D interconnected structure was maintained (Fig. S6), thus indicating excellent structural stability. The above results suggest that N doping can facilitate ion

Fig. 4 **a** CV curves; **b** Galvanostatic charge/discharge curves; **c** Specific capacitance; and **d** Cycle stability of the 2D N-NiO UTNSs electrode



transfer from the electrode and electrolyte for the (non)faradaic reaction, while ultrathin 2D structures facilitate electron transfer and thus enhance electrochemical performance. Moreover, the interconnected ultrathin 2D structures guarantee the preservation of structural integrity during long-term charge/discharge cycling.

Response time is an important parameter of electrochromic materials and is usually defined as the time required to achieve 90% of the total transmittance modulation [27]. Herein, response time was measured at 550 nm under the application of a square-wave voltage between -0.3 and 0.7 V vs. Hg/HgO (Fig. 5a) and equaled 5.47 and 3.67 s for the bleached and colored states of N-NiO UTNSs, respectively. Coloration efficiency (CE), another important parameter of electrochromic materials, can be expressed as [28]:

$$CE = \Delta OD / \Delta Q, \Delta OD = \log(T_b / T_c), \quad (2)$$

where T_b and T_c are the transmittances of bleached and colored states, respectively, ΔOD is optical density change, and ΔQ is a function of insertion/extraction charge [29]. The CE of N-NiO UTNSs at 550 nm was calculated as $83.47 \text{ cm}^2 \text{ C}^{-1}$ from the slope of the quasi-linear portion of the dependence of ΔOD on charge density (Fig. 5b). These results confirmed that N doping and the presence of an interconnected ultrathin 2D structure facilitate ion transport and electron transfer, thus shortening the response time and ensuring excellent CE.

It remains challenging to achieve both high supercapacitance performance and electrochromic performance because of the basic contradiction of energy storage and electrochromism [30]. Comparing the supercapacitance and electrochromic

performance with the present status and literature survey on NiO-based ESCs (presented in the Table 1) [8, 14, 31–33], our design of the ESCs electrode was proved to be a powerful way to achieve both high supercapacitance performance and electrochromic performance.

Finally, we constructed an AESC using 2D N-NiO UTNSs and Fe_2O_3 as positive and negative electrodes, respectively (Scheme 1). Prior to integration, Fe_2O_3 and N-NiO UTNSs were subjected to CV tests in 1 M KOH in a three-electrode system at a scan rate of 5 mV s^{-1} . As shown in Fig. S7, the working potential windows of Fe_2O_3 and N-NiO UTNSs were -1 to 0 V and 0 to 0.7 V vs Hg/HgO, respectively, which suggested that the operation potential of our AESC can reach 1.7 V.

The AESC charge state was directly reflected by color, in line with the requirement of smart electrochromic supercapacitors. To prove the suitability of our AESC for intelligent visualization applications, we recorded its color changes during charge/discharge. As shown in Fig. 6a, the AESC exhibited “colorless \leftrightarrow light brown \leftrightarrow brown \leftrightarrow dark brown” color changes as the voltage increased from 0 to 1.7 V and was also characterized by fast coloration and bleaching (Video S1). Two charged AESCs (dark brown) connected in series could light up a red light-emitting diode (Fig. 6b) that went out upon discharge (Fig. 6c), which was accompanied by the above color change (Video S2). These results indicated that the developed AESC is well suited for the intelligent visualization of energy storage state.

Fig. 5 **a** Transmittance-time profile of the 2D N-NiO UTNSs electrode at 550 nm; **b** Optical density versus charge density of the 2D N-NiO UTNSs electrode

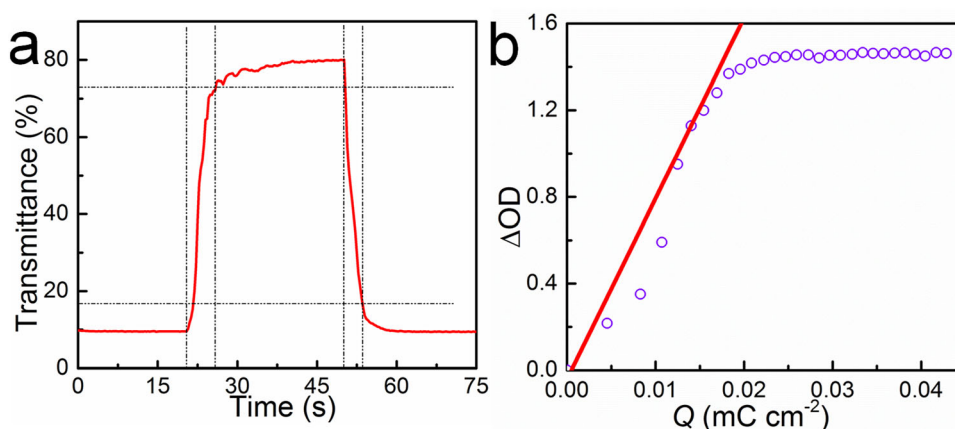
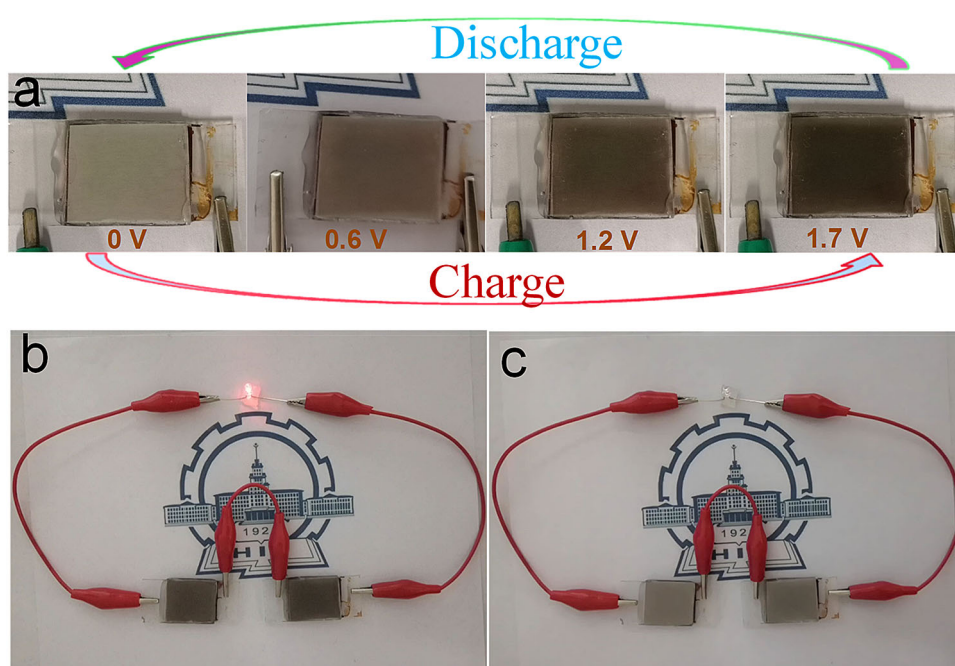


Table 1 Present status and literature survey of electrochromic supercapacitor

Sr. no.	Optical modulation (%)	Coloration efficiency (cm ² C ⁻¹)	Specific capacitance	Cycling stability (%), cycle numbers	Ref no.
1	63.6	42.8	1386 F g ⁻¹ (on nickel foam)	78.5, 5000	[8]
2	35	30.6	–	100, 100	[31]
3	24.3	76.6	364.0 F g ⁻¹	89.3, 500	[32]
4	20	10.8	12 C g ⁻¹	–	[14]
5	55.6	45.9	543 F g ⁻¹	90, 5000	[33]
Our work	73	83.47	540 F g ⁻¹	85, 10,000	

Fig. 6 **a** Digital photos of the ASC window showing different colors when different voltages are applied; **b** and **c** photo of a red LED lit up and out by two series-connected ASCs



4 Conclusion

Two-dimensional N-doped NiO ultrathin nanosheets were prepared via a single-step solvothermal reaction followed by simple annealing in the absence of a nitrogen source. N doping increased the electronic conductivity of NiO, and the ultralow nanosheet thickness resulted in shorter ion diffusion paths for the NiO electrode and the electrolyte, thus ensuring excellent electrochromic and supercapacitor performances. The prepared nanosheets were used to construct an intelligent AESC that could light a light-emitting diode and exhibited charge state-dependent color, which allowed the charge state to be monitored in real time.

Acknowledgements

We thank National Key Research & Development Program (2016YFB0303903, 2016YFE0201600) and Foundation of Equipment Development Department (6220914010901). We would like to thank Editage (www.editage.cn) for English language editing.

Electronic supplementary material: The online version of this article (<https://doi.org/10.1007/s10854-020-04581-3>) contains supplementary material, which is available to authorized users.

References

- Z. Xie, Q. Zhang, Q. Liu, J. Zhai, X. Diao, *Thin Solid Films* **653**, 188 (2018)
- Q. Guo, J. Li, B. Zhang, G. Nie, D. Wang, *ACS Appl. Mater. Interfaces* **11**, 6491 (2019)
- S. Qin, Q. Zhang, X. Yang, M. Liu, Q. Sun, Z.L. Wang, *Adv. Energy Mater.* **8**, 1 (2018)
- J. Li, Q. Guo, Y. Lu, G. Nie, *Eur. Polym. J.* **113**, 29 (2019)
- S. Cong, Y. Tian, Q. Li, Z. Zhao, F. Geng, *Adv. Mater.* **26**, 4260 (2014)
- Z. Tong, N. Li, H. Lv, Y. Tian, H. Qu, X. Zhang, J. Zhao, Y. Li, *Sol. Energy Mater. Sol. Cells* **146**, 135 (2016)
- S. Mishra, P. Yogi, P.R. Sagdeo, R. Kumar, *ACS Appl. Energy Mater.* **1**, 790 (2018)
- G. Cai, X. Wang, M. Cui, P. Darmawan, J. Wang, A.L.S. Eh, P.S. Lee, *Nano Energy* **12**, 258 (2015)
- Y. Shi, Y. Zhang, K. Tang, J. Cui, X. Shu, Y. Wang, J. Liu, Y. Jiang, H.H. Tan, Y. Wu, *Chem. Eng. J.* **355**, 942 (2019)
- L. Li, J. Zhang, J. Lei, J. Xu, B. Shang, L. Liu, N. Li, F. Pan, *J. Mater. Chem. A* **6**, 7099 (2018)
- Y. Li, Y. Cui, Z. Yao, G. Liu, F. Shan, *Scr. Mater.* **178**, 472 (2020)
- D. Liang, S. Wu, J. Liu, Z. Tian, C. Liang, *J. Mater. Chem. A* **4**, 10609 (2016)
- Y. Feng, H. Zhang, Y. Zhang, Y. Bai, Y. Wang, *J. Mater. Chem. A* **4**, 3267 (2016)
- H.K. Jung, S.J. Lee, D. Han, A.R. Hong, H.S. Jang, S.H. Lee, J.H. Mun, H.J. Lee, S.H. Han, D. Yang, D.H. Kim, *Electrochim. Acta* **330**, 135203 (2020)
- L. Zhu, C.K. Nuo Peh, T. Zhu, Y.F. Lim, G.W. Ho, *J. Mater. Chem. A* **5**, 8343 (2017)
- M. Acerce, D. Voiry, M. Chhowalla, *Nat. Nanotechnol.* **10**, 313 (2015)
- P. Liu, M. Yang, S. Zhou, Y. Huang, Y. Zhu, *Electrochim. Acta* **294**, 383 (2019)
- B. Xia, T. Wang, X. Jiang, J. Li, T. Zhang, P. Xi, D. Gao, D. Xue, *J. Mater. Chem. A* **7**, 4729 (2019)
- M. Yu, Z. Wang, C. Hou, Z. Wang, C. Liang, C. Zhao, Y. Tong, X. Lu, S. Yang, *Adv. Mater.* **29**, 1602868 (2017)
- K. Choi, I.K. Moon, J. Oh, *J. Mater. Chem. A* **7**, 1468 (2019)
- J.H. Zhang, G.F. Cai, D. Zhou, H. Tang, X.L. Wang, C.D. Gu, J.P. Tu, *J. Mater. Chem. C* **2**, 7013 (2014)
- X.P. Yang, J.G. Lu, H.H. Zhang, Y. Chen, B.T. Kan, J. Zhang, J. Huang, B. Lu, Y.Z. Zhang, Z.Z. Ye, *Chem. Phys. Lett.* **528**, 16 (2012)
- D. Han, X. Jing, J. Wang, P. Yang, D. Song, J. Liu, *J. Electroanal. Chem.* **682**, 37 (2012)
- M.C. Biesinger, B.P. Payne, L.W.M. Lau, A. Gerson, R.S.C. Smart, *Surf. Interface Anal.* **41**, 324 (2009)
- T. Dutta, P. Gupta, A. Gupta, J. Narayan, *J. Appl. Phys.* **108**, 083715 (2010)
- D. Su, S. Dou, G. Wang, *Adv. Energy Mater.* **5**, 1 (2015)
- D. Zhou, B. Che, X. Lu, *J. Mater. Chem. C* **5**, 1758 (2017)
- X. Zhang, S. Dou, W. Li, L. Wang, H. Qu, X. Chen, L. Zhang, Y. Zhao, J. Zhao, Y. Li, *Electrochim. Acta* **297**, 223 (2019)
- D.S. Dalavi, R.S. Devan, R.S. Patil, Y.R. Ma, M.G. Kang, J.H. Kim, P.S. Patil, *J. Mater. Chem. A* **1**, 1035 (2013)
- P. Yang, P. Sun, W. Mai, *Mater. Today* **19**, 394 (2016)
- Y. Liu, C. Jia, Z. Wan, X. Weng, J. Xie, L. Deng, *Sol. Energy Mater. Sol. Cells* **132**, 467 (2015)
- W. Dong, Y. Lv, N. Zhang, L. Xiao, Y. Fan, X. Liu, *J. Mater. Chem. C* **5**, 8408 (2017)
- A.I. Inamdar, H.S. Chavan, H. Kim, H. Im, *Sol. Energy Mater. Sol. Cells* **201**, 110121 (2019)

Publisher's Note Springer Nature remains neutral with regard to jurisdictional claims in published maps and institutional affiliations.